Thermal stability of the lightweight 2099 Al-Cu-Li alloy: tensile tests and microstructural investigations after overaging T83

E. Balducci [a*], L. Ceschini [a]

[a] Dept. of Industrial Engineering, Alma Mater Studiorum University of Bologna, via del Risorgimento 2, Bologna, Italy

* corresponding author: eleonora.balducci6@unibo.it, phone number +393477175235

S. Messieri [b]

[b] Ducati Motor Holding, Bologna, Italy

S. Wenner [c], R. Holmestad [c]

[c] Dept. of Physics, Norwegian University of Science and Technology, Høgskoleringen 5, Realfagbygget D4-153, Trondheim, Norway

Highlights

- Lightweight AA2099(Al-Cu-Li) exhibits a thermal stability comparable or even higher than other Al-Cu alloys specifically developed for high temperature applications.
- Overaged AA2099 showed high residual hardness and tensile strength, suggesting its potential use in high temperature (yet lighter) automotive components.
- STEM investigations revealed the superior thermal stability of the T_1 phase (typical of Al-Cu-Li alloys) compared to ϑ and S.

Abstract

The thermal stability of the lightweight, T83 heat treated 2099 Al-Cu-Li alloy was assessed in the temperature range 200-305°C, through both hardness and tensile tests. After prolonged overaging, the alloy exhibited a better performance compared to aluminium alloys specifically developed for high temperature applications, with the advantage of a considerable lower density. The tensile behaviour was modelled through Hollomon's equation as a function of residual hardness. The changes in the alloy performance were explained through both SEM and STEM investigations.

Microstructural analyses gave evidence of Ostwald ripening, while fractographic analyses revealed a transition from an intergranular to a ductile fracture mechanism in the overaged alloy. STEM investigations highlighted the superior thermal stability of the T_1 phase compared to ϑ and S strengthening phases, which dissolved during overaging at 245°C. The study underlines the need to enhance the formation of T_1 precipitates when high temperature strength is required. The results of the present study suggest that the 2099 alloy is a very promising candidate for automotive engine components, which are extremely demanding in terms of both thermal resistance and lightweight.

Graphical abstract

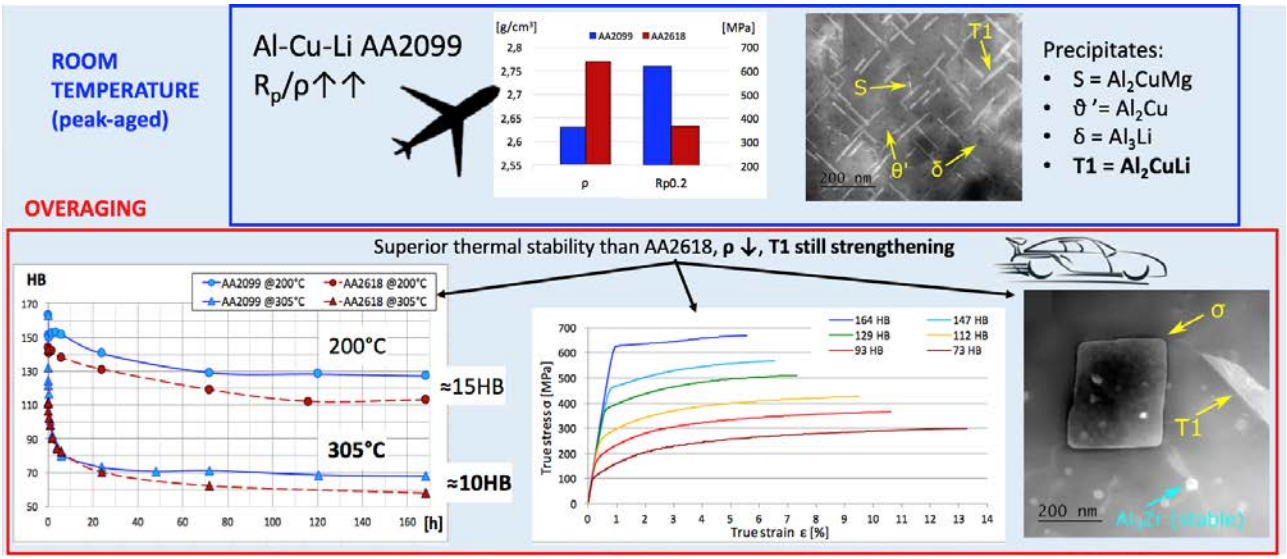

Keywords

Al-Cu-Li alloy; Thermal effect; Hardness test; Tensile test; Microstructure; STEM.

1. Introduction

The 2099 Al alloy belongs to the third generation of Al-Li alloys, which are high performance and lightweight materials. Lithium exhibits the lowest density among metals, equal to 0.534 g/cm^3, hence it significantly contributes to a density reduction of the alloy. The substantial influence of Li

addition in density reduction was at first underlined by Peel et al. [1] in the empirical formula to calculate Al alloy densities (Equation 1).

$$\rho\ (g/cm^3) = 2.71 + 0.024Cu + 0.018Zn + 0.022Mn - 0.01Mg - 0.004Si - \mathbf{0.079Li}$$

Equation 1: Empirical formula to evaluate the density of Al alloys; atomic symbols represents the concentration of the element in wt%. The benefit of Li addition is clearly visible [1].

Another relevant aspect is that Li increases the Young's elastic modulus of the alloy (around 6% increase due to 1wt% Li addition [2]). Combined with the possibility to use conventional production processes, the enhancements in specific strength and stiffness have made Al-Li alloys a competitive alternative to more conventional aluminium alloys (such as those of the 6XXX and 7XXX series) for structural applications in the aerospace field [3–7], due to the consistent improvements in payload and fuel efficiency.

Rioja et al. [2,8] offered a comprehensive review on the microstructural and technical issues which finally lead to the development of the complex third generation of Al-Li alloys. Starting from the first generation, a significant enhancement in fracture toughness has been achieved thanks to both a specific balance in chemical composition and a simultaneous optimization of the thermo-mechanical processing. To obtain the maximum benefits in terms of mechanical properties, Al-Li alloys need to be processed to the T8 condition (solution, quench, cold stretch, artificial aging), the key point being the generation of the desired texture and sub-structure to make the precipitation more effective and uniform [9,10]. Cold deformation, in fact, induces a dislocation network which acts as nucleation site for co-precipitation of strengthening intermetallics (mainly Cu and Li based); the result is, therefore, both a refinement of precipitates microstructure and a reduction in precipitation at grain boundaries, which is deleterious in terms of toughness [2,11]. Together with an increased Cu/Li ratio, T8 heat treatment promotes the formation of the T_1 (Al_2CuLi) phase at the expenses of δ' (Al_3Li) precipitates [2,12–16], which offers the maximum strengthening effect and is more thermally stable. In addition to these strengthening phases, the relevant presence of Cu and

Mg in Al(-Cu)-Li alloys leads to the formation of θ' (Al_2Cu), S' (Al_2CuMg) and σ ($Al_5Cu_6Mg_2$) phases.

Usually, Zr and Mn are also added in low quantities; these elements are known to form Al_3Zr (spherical) and $Al_{20}CuMn_3$ (rod-like shaped) dispersoids, essential to control texture, to pin grain and sub-grain migration and to inhibit recrystallization, enhancing fracture toughness [2,11,17–19]. Given the opposite microsegregation patterns of Mn and Zr in Al, the joint addition of these elements is thought to produce a more uniform dispersion coverage, even if recent studies highlighted a reduction in recrystallization resistance [18].

An overview of the microstructural features of the 2099 Al-Cu-Li alloy is offered by Rioja et al. in [2], whose schematic is reported in Fig.1. Further in-depth microstructural investigations are present in literature, which confirm the abovementioned features and characteristics of both strengthening precipitates and dispersoids [11,20,21].

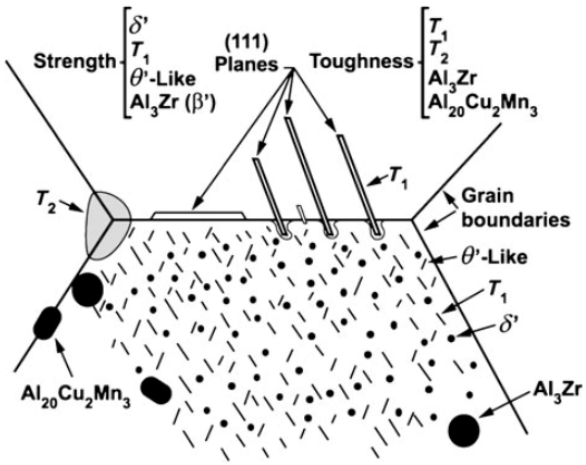

Figure 1: Schematic of Al-Cu-Li 2099 alloy microstructural features, focusing on precipitates and dispersoids [2]. *Reprinted under Springer permission.*

Since the '80s, several studies have been carried out on T8 heat treated AA2099, due to its interesting properties for aerospace applications, however there is a substantial lack of studies focusing on the thermal stability of this alloy. Very few studies, whose aim is mainly linked to the

design of the aging treatment, deal with thermal exposure of AA2099 at medium-high temperature (that is below 200°C), but little attention has been given to microstructural features [15,20,22,23]. Jabra et al. [24] firstly evaluated the response of AA2099 to prolonged thermal exposure at elevated temperatures (180°C, 230°C, 290°C), in order to replicate a range of possible thermal environments. For all the investigated temperatures, a decrease of tensile properties was found, coupled with an increase of the elongation to failure. Even if the decay of tensile properties showed a good correlation with residual hardness data, no systematic relationship was determined. Moreover, up to date, there is a total lack of microstructural investigations on the high temperature overaging of the AA2099 alloy, which still raises open questions about the thermal stability of its precipitates, or about which type of precipitates are needed during the aging treatment in case of high temperature applications.

Further studies are therefore required in order to completely characterise the alloy strengthening mechanisms and, above all, to evaluate the maximum service temperature the alloy is able to withstand without a significant strength loss. The study falls within a wider context: the huge benefits of AA2099 in terms of mass savings make it a potential candidate not only for structural components in the aerospace field, but also for automotive applications, even for engine components. The increasingly topical race to boost fuel economy, which today involves car manufacturers, has not to be neglected. Since automotive applications are extremely challenging in terms of both specific strength and service temperature, the aim of this study is to evaluate the possibility to expand the 2099 temperature range of applications. Time-Temperature-Hardness curves, tensile tests at room and high temperature on peak-aged and overaged samples, and microstructural investigations through both Scanning and Transmission Electron Microscopy have been carried out, in order to outline the microstructural modifications which mainly affect the mechanical behaviour of the alloy.

2. Experimental

The material used in the present study was a 2099 Al-Cu-Li alloy, provided by Alcoa in the form of extruded bars with 85mm diameter. The alloy was industrially heat treated according to the T83 condition (which consists of solution treatment, quench, 3% stretching at room temperature followed by artificial aging). The chemical composition limits of AA2099, provided by the supplier, are reported in Table 1.

Cu	**Li**	Zn	Mn	Mg	Ti	Zr	Fe	Others, each	Others, tot	Al
2.4-3.0	**1.6-2.0**	0.40-1.0	0.10-0.50	0.10-0.50	0.10	0.05-0.12	0.07	0.05	0.15	Bal.

Table 1: Chemical composition limits [wt%] of AA2099.

In order to assess the thermal stability of the alloy, several specimens (10x15x6) mm^3 in size, were cut from the T83 extruded bar. The samples were then subjected to different overaging heat treatments in the temperature range 200-305°C, the soaking time ranging from 2min up to 168h. Additional overaging curves at lower temperatures (155-185°C) were added to the analyses, aiming to determine the maximum temperature the alloy is able to withstand without any loss of properties; for this purpose, the soaking time was reduced to 24h. During the heat treatments, the temperature of the samples was controlled by a K-type thermocouple, allowing ± 2°C variation of the targeted temperature. For each time-temperature condition, the residual hardness of the alloy was determined as the average of 6 hardness measurements, performed on 2 different samples. Brinell hardness tests were carried out according to the ASTM E 10-08 standard, the indenter being a hardened steel ball, 2.5mm in diameter, and the applied load being equal to 62.5kg.

The microstructural characterisation of T83 and over-aged alloy was carried out on samples mechanically ground with SiC papers to 4000 grit and finally polished up to 0.05µm colloidal silica. Chemical etching through Keller's reagent (95mL H_2O, 2.5mL HNO_3, 1.5mL HCl, 1mL HF) was then carried out in order to perform Optical Microscopy (OM) analyses, while Scanning

Electron Microscopy (SEM) analyses and Energy Dispersive Spectroscopy (EDS) investigations were carried out on not-etched samples.

Once the minimum residual Brinell hardness of the alloy has been determined through overaging curves, the interval between the maximum hardness value (characterising the T83 condition) and the minimum value was divided into 6 equally spaced hardness classes, in order to study the variation of tensile properties due to thermal exposure. It is in fact widely accepted that mechanical properties of Al alloys deteriorate during thermal exposure, and a nearly-linear relationship exists between the softening of the alloy and the decrease of its tensile properties [25]. With the aim to reach the targeted residual hardness for each class, specific overaging heat treatments were performed on tensile specimens, the time-temperature parameters being selected according to the previous overaging results. Room temperature tensile tests were then carried out on both T83 and overaged samples, using a screw tensile testing machine. Test parameters and geometry of samples were defined according to EN ISO 6892-1: 2009 standard; the strain rate was set equal to $3.3x10^{-3}\ s^{-1}$; the specific dimensions of the tensile samples are reported in Fig.2.

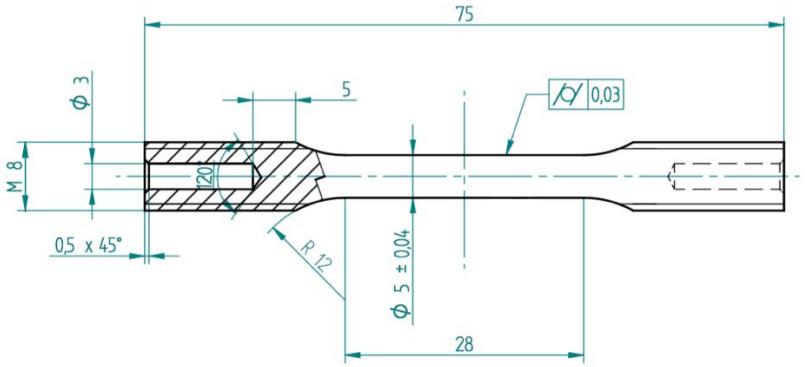

Figure 2: Geometry and dimensions [mm] of tensile specimens.

Proof strength ($Rp_{0.2}$), ultimate tensile strength (UTS) and elongation to failure (A_t%) were evaluated according to EN ISO 6892-1: 2009 standard; the representativeness of the results was assured by testing 3 specimens for each class of residual Brinell hardness. To accurately establish

the relationship between the average values of UTS, $Rp_{0.2}$, A_t% and residual hardness, the targeted residual hardness was confirmed by Brinell hardness tests, performed on grip areas of tensile samples after testing.

In order to completely describe the flow behaviour at room temperature, the true stress–true strain (σ-ε) curves referring to different overaging conditions have been also modelled according to Hollomon's equation [26]:

$$\boldsymbol{\sigma = K\varepsilon^{n}}$$

Equation 2: Hollomon's law, representative of the behaviour of the alloy in the plastic field, when deformation occurs at room temperature [26].

The strength coefficient K and the hardening coefficient n were evaluated according to ISO 10275:2007 standard, taking into account true stress-true strain data between 2% plastic strain and the percentage plastic extension at maximum force (A_g). Since the purpose was to outline the changes in the alloy behaviour due to thermal exposure, K and n values have been modelled as a function of the residual hardness of tensile samples.

In order to relate experimental results with microstructural changes, SEM analyses of the fracture surfaces were carried out, using both secondary and backscattered electrons. Finally, to investigate how the density, size and type of precipitates evolve during overaging, annular dark-field scanning transmission electron microscopy (ADF-STEM) studies were conducted. Samples were prepared by grinding the material to 100 μm thin foils, which were punched to 3mm discs. The discs were electropolished using a TenuPol-5 unit and an electrolyte containing 1/3 HNO_3 and 2/3 CH_3OH, cooled down to −25 °C. The applied voltage was 20V. The ADF-STEM images were acquired on a JEOL JEM-2100F microscope, operated at 200kV. Samples were imaged both in $<001>_{Al}$ and $<112>_{Al}$ directions for identification of all the phases present.

3. Results and discussion

3.1 Starting material

The as-received alloy was characterised both by OM and SEM-EDS investigations. Representative OM micrographs, both in the longitudinal and transverse directions, are reported in Fig.3, and reveal the typical unrecrystallized microstructure of T8 Al-Cu-Li alloys [2,3,11,27,28], with grains elongated along the extrusion direction.

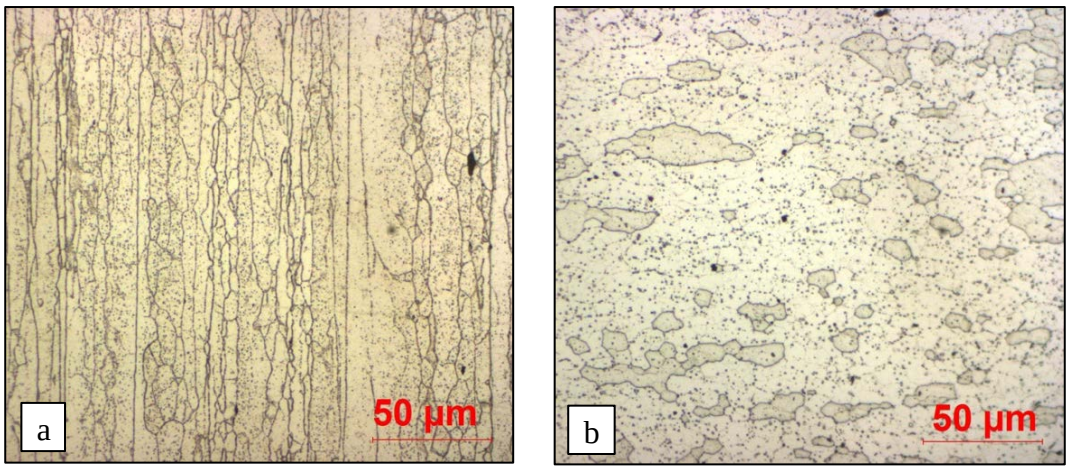

Figure 3: OM micrographs of the T83 AA2099, after chemical etching by Keller's reagent: (a) longitudinal and (b) transverse directions.

This morphology is confirmed by SEM investigations on T83 alloy (Fig.4a), which show secondary phases aligned towards the extrusion direction. Consistent with observations by Ma et al. [11], EDS analyses reveal that the secondary phases mainly consist of Al-Mn-Fe-Cu, and that brighter areas are richer in Cu (Fig.4b). Due to the very fine size of coherent precipitates and dispersoids, characterising the 2099 alloy in the T83 condition, SEM investigations were not able to resolve other microstructural features.

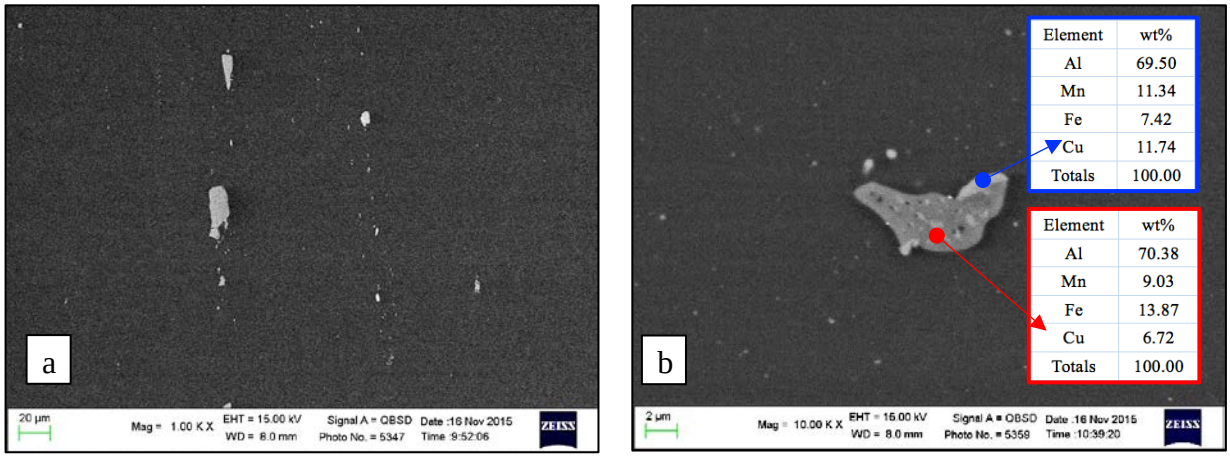

Figure 4: SEM-EDS analyses of AA2099 in the T83 condition at (a) low and (b) high magnification, with focus on Al-Mn-Fe-Cu secondary phases.

3.2 Time – Temperature – Hardness curves

The complete overaging curves, obtained in the range 200–305°C for soaking time up to 168h, are reported in Fig.5a. Lower temperatures (155–185°C) were also investigated for shorter soaking time, up to 24h, and the results are reported in Fig.5b. To have a more effective comparison with curves at higher temperatures, also the curve at 200°C was here reported in solid line.

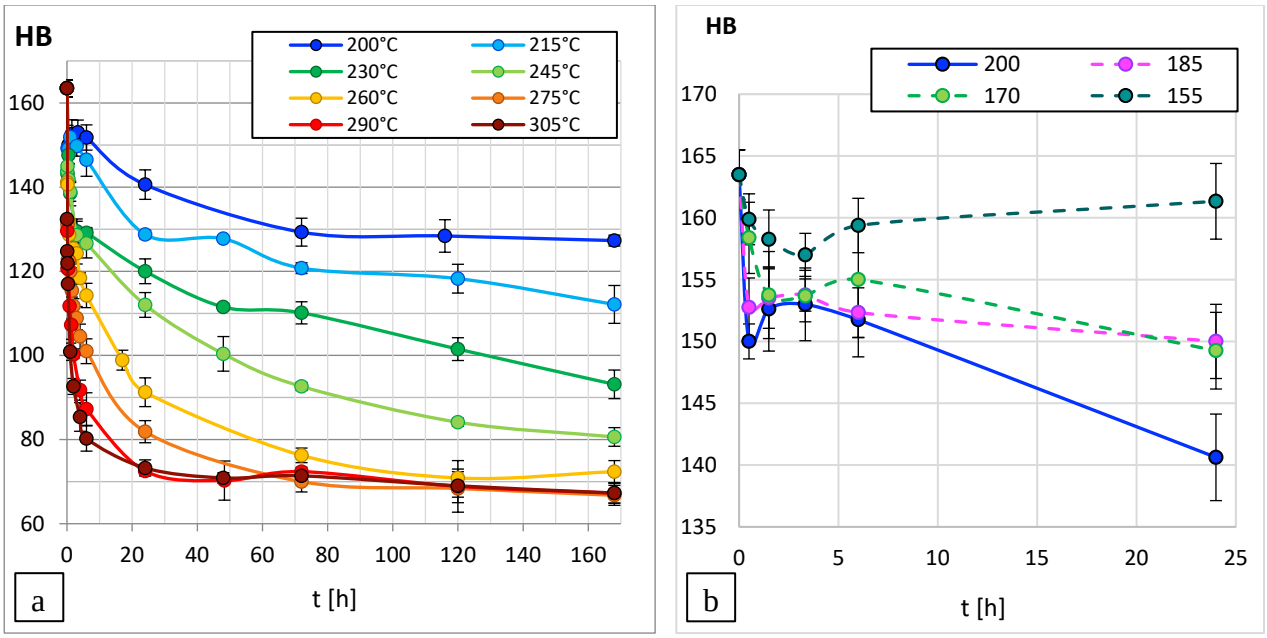

Figure 5: Overaging curves referring to AA2099; each point is obtained as the average of 6 Brinell hardness values; error bars are representative of 95% confidence interval (±2σ). (a) Overaging curves in the range of interest (200-305°C) to assess the thermal stability of the alloy. (b) Overaging curves in the range 155-180°C with a reduced soaking time, aimed to determine the maximum temperature which does not produce softening; part of 200°C overaging curve (solid line) is also reported, to make an effective comparison with the additional overaging curves at 155-185°C (dashed lines).

Since the softening of the alloy consists of a diffusion-controlled mechanism, the strength loss is more pronounced and it occurs faster at higher temperatures. Fig.5a, however, reveals that the thermal stability of the alloy is compromised even at temperatures which are usually considered relatively low in the automotive field; in fact, the high hardness value in the T83 condition, equal to 164HB, is immediately lost after only 30 min of exposure at 200°C.

The additional overaging curves at lower temperatures, separately reported in Fig.5b, allowed to determine the maximum temperature that does not significantly affect the alloy strength. It can be noted that the hardness of the T83 alloy is almost maintained even after 24h of soaking time at 155°C; it can therefore be stated that no substantial microstructural evolution occurs at this temperature, since the driving force for the diffusion processes is extremely low. The slight instability which occurs for short time of exposure at low temperature, barely detectable at 155°C, is in all probability connected to the little coarsening of δ' precipitates, since the hardness variation is actually limited and the typical Al-Cu based precipitates (ϑ' and S) do not tend to coarsen at this

low temperature. The hypothesis is in agreement with Lin et al. [20], who demonstrated that slight overaging occurred even with prolonged time (96h) at 152°C, due to little coarsening of δ' precipitates.

Ortiz et al. [22] confirmed that tensile properties remain substantially stable up to 1000h of exposure at 83°C and 135°C, while a relevant decrease of strength is detected when the alloy is exposed to 177°C, up to 1000h; the same observation is supported by Romios et al. [23] and Gao et al. [15], who considered the soaking at 180°C responsible for overaging.

A plateau of hardness, equal to about 70HB is reached when the 2099 alloy is maintained at temperatures equal to or higher than 260°C, as shown in Fig.5a. Due to its thermodynamically driven nature, the softening is faster at 290°C and 305°C, temperatures at which 24h is the required time to complete the microstructural evolution and to reduce the driving force for the coarsening of precipitates (Ostwald ripening).

Additional SEM analyses carried out on the overaged samples are reported in Fig.6 and gave evidence of microstructural evolution, which significantly depends on temperature and time of exposure. The consequences of Ostwald ripening are in fact clearly visible by comparing the SEM micrographs reported in Fig.4b and Fig.6a-b, obtained with the same magnification. Due to an increase in temperature (or time) of exposure, a network of coarse precipitates starts to decorate grain or sub-grain boundaries and finally it tends to cover the matrix itself.

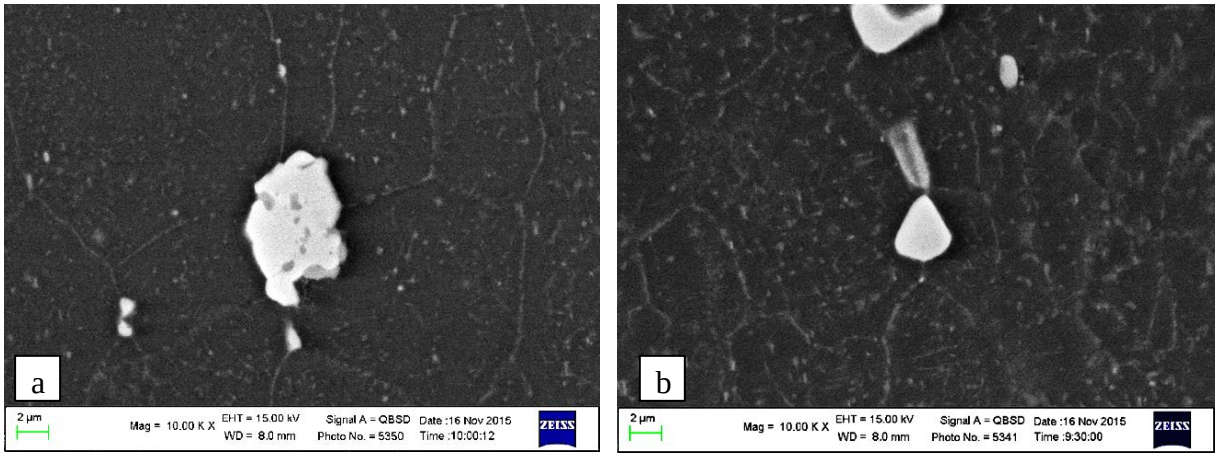

Figure 6: SEM micrographs of the overaged samples, after 24h soaking time at (a) 245°C and (b) 305°C, same magnification.

The coarsening of strengthening precipitates is unavoidable in heat treated aluminium alloys. However, in order to enlighten the potentiality of AA2099 in terms of thermal resistance, it is worth making a comparison with another high temperature resistant Al-Cu alloy, such as the AA2618:

- AA2099 contains Li and its peculiarity it the extremely low density and good mechanical properties at room temperature, both favouring its main applications in the aerospace field.
- AA2618 contains significant amount of Ni and Fe, and it is specifically developed for high temperature applications in the automotive field.

By comparing the two alloys in the most overaged condition (exposure at 305°C for 168h), it is worth underlining that the residual hardness of the 2099 alloy (about 70HB) is still higher than that of the AA2618 (about 60HB, as reported by Ceschini et al. [25]). This result further strengthens the hypothesis that AA2099 can be suitable for automotive components running at high temperature, yet exhibiting a lower density.

3.3 Scanning Transmission Electron Microscopy analyses

Along with the T83 condition (164 HB), samples overaged for 24h at 245°C (residual hardness ≈ 110 HB) and 305°C (residual hardness ≈ 70 HB) were selected for STEM analysis, in order to study

the peak-aged condition and the microstructural changes responsible of the slightly overaged and heavily overaged conditions. The decision process was driven by the results of the overaging curves reported in Fig.5a, which show that the 3 selected samples are evenly spaced in the range of residual hardness investigated in this study. It should be underlined that the hardness plateau equal to 70HB is reached after just 24h at 305°C, and that hardness does not significantly change by further prolonging the time of exposure at 305°C. Since hardness and tensile properties are interrelated, and both strictly connected to microstructural changes, it can be inferred that the microstructural evolution responsible of overaging already occurred after 24h at 305°C. The latter condition was therefore considered as representative of the mostly overaged investigated condition. Fig.7 shows the collected STEM images.

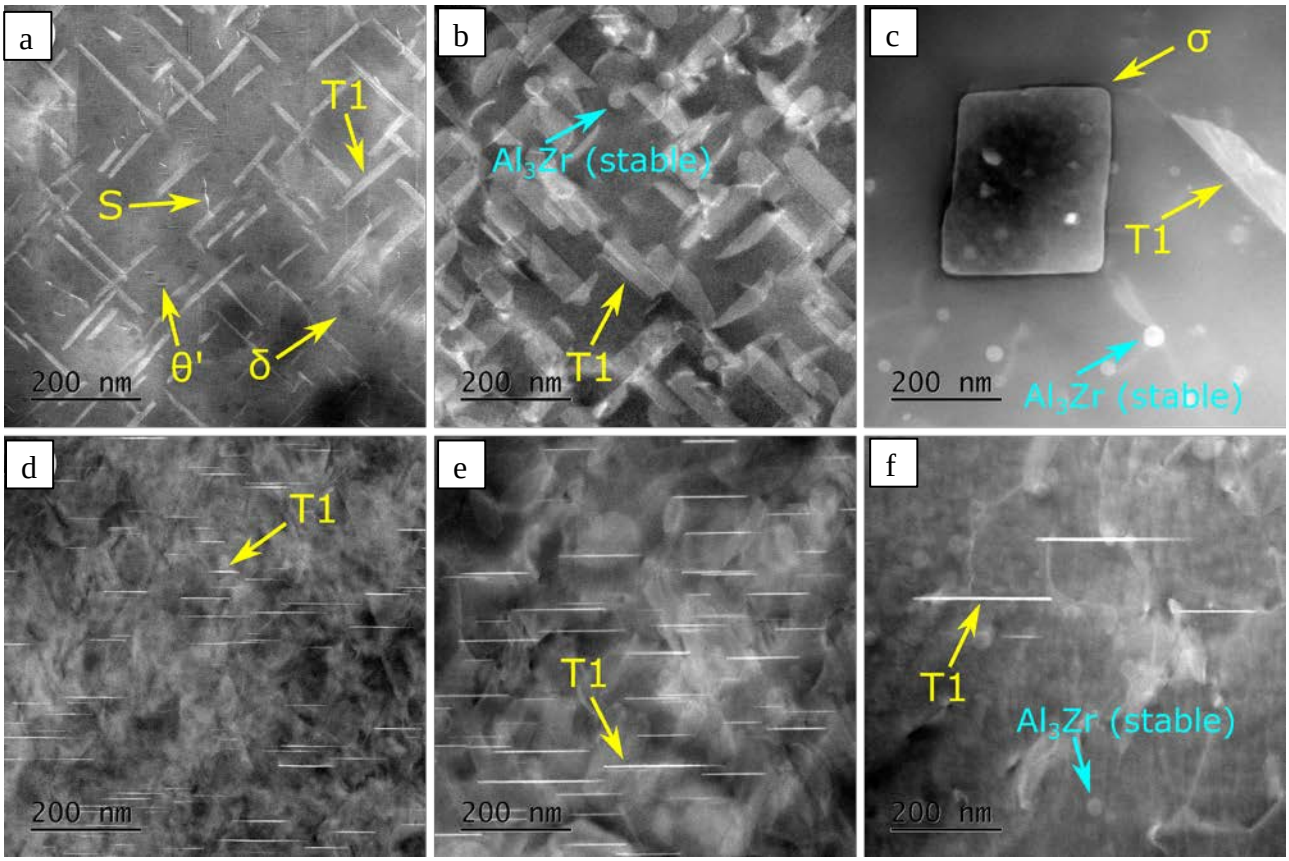

Figure 7: ADF-STEM images of the precipitate microstructure in (a),(d) the T83 condition, (b),(e) overaged at 245°C for 24h and (c),(f) overaged at 305°C for 24h. (a),(b),(c) are acquired along the <001>Al direction and (d),(e),(f) in the <112>Al direction.

In the T83 condition, the ADF-STEM images (Fig.7a,d) show a fine, rich precipitate microstructure with Cu-containing phases (S, T_1 and ϑ' phase) appearing bright and the Li-containing δ phase appearing dark, because the atomic weights of these elements are very different from that of Al. Apart from T_1, all strengthening phases dissolve upon overaging at 245°C for 24h, while T_1 continues to exist and grows in thickness (Fig.7b,e). According to Gao et al. [15], just prolonging the aging time at 200°C to 72h is sufficient to dissolve δ' and θ', while the T_1 and S phases still remain stable.

Even at the highest overaging temperature considered in the present investigation (305°C) a coarser distribution of T_1 particles is perceivable, as indicated in Fig.7c,f. This aspect confirms that the T_1 phase, which contains both Cu and Li, is the main responsible for the remarkable thermal stability of Al-Cu-Li alloys. The coarse and incoherent σ phase is formed at high temperatures (it is evident in the alloy overaged for 24h at 305°C, as highlighted in Fig.7e) and does not contribute to strengthening. In agreement with [33], the cubic structured σ phase is usually observed in overaged Al-Cu-Mg alloys, and it corresponds to the stoichiometric formula $Al_5Cu_6Mg_2$. It is however reported in literature [15,34] that cubic σ phase might also form in Al-Cu-Li alloys in different aging or overaging conditions.

EDS maps were also performed on the most overaged sample, as reported in Fig.8, in order to combine chemical and morphological analyses and to clearly define the phases still present after overaging. It is worth to point out that the EDS maps reveal the presence of significant amount of Cu and Mg coupled with Zn in the cubic phase. The presence of Zn is in agreement with the theory proposed by Li et al. [34], aiming to explain the formation of σ phase in absence of Si or Ag: Zn is suspected to contribute to its nucleation. According to literature data [15,34], thermal exposure leads to overaging of all the strengthening precipitates characterising the 2099 Al-Cu-Li alloy, with

the exception of the σ phase. However, the coarse dimensions of the σ phase and its incoherency with the Al matrix prevent it from providing a consistent strengthening effect.

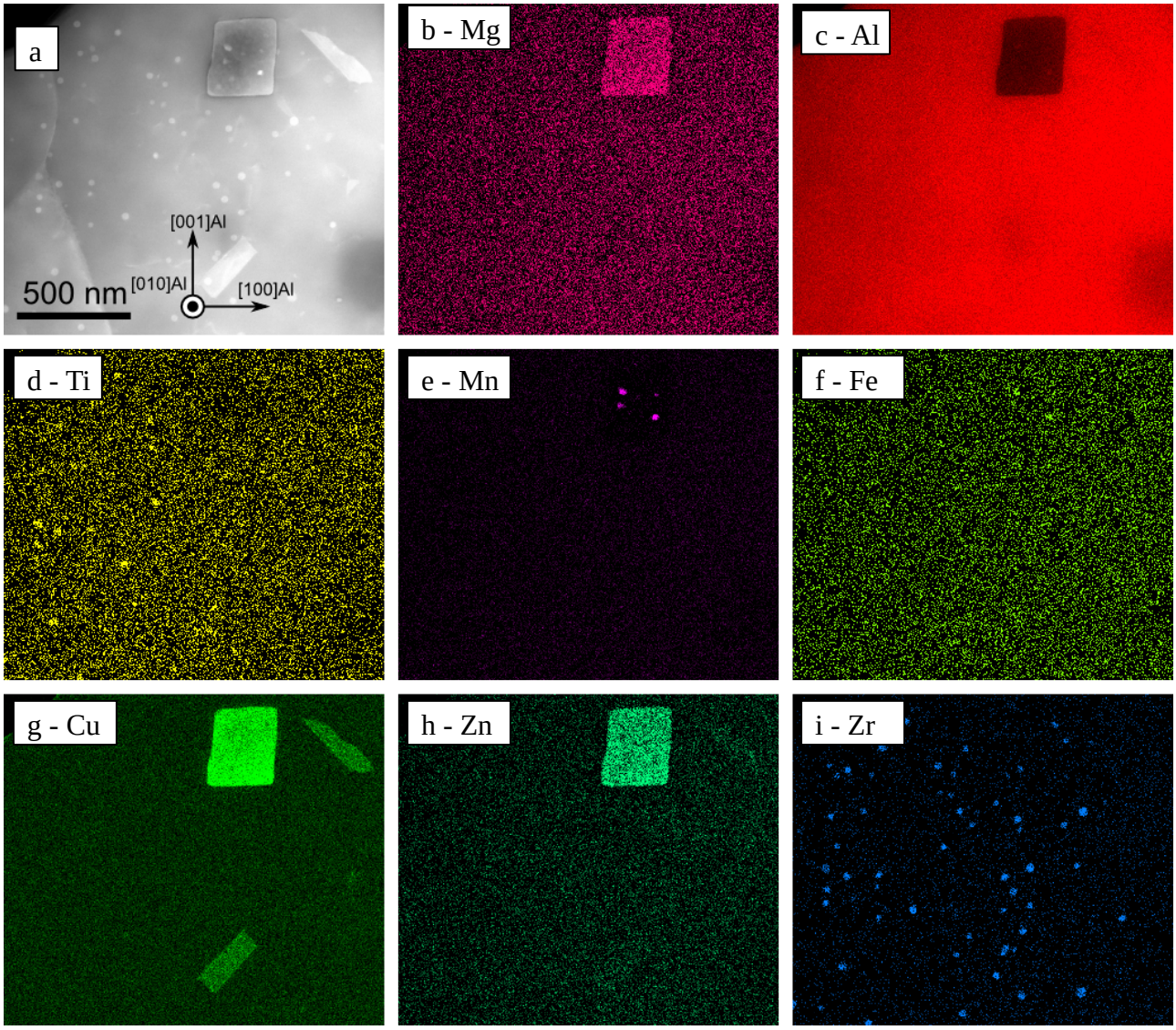

Figure 8: ADF-STEM image of the precipitate microstructure overaged at 305°C for 24h, acquired along the <001>Al direction (a), and corresponding EDS mapping of Mg (b), Al (c), TI (d), Mn (e), Fe (f), Cu (g), Zn (h), Zr (i).

3.4 Tensile tests

Based on the hardness interval determined by the overaging curves (roughly equal to 100HB, between the T83 condition and the minimum hardness value of 67HB, which is reached after 168h at 305°C), 6 hardness classes were defined for the tensile specimens: peak-aged (164HB), 147HB, 129HB, 112HB, 93HB, 73HB. Among the possible couples of time-temperature conditions to reach

the targeted residual hardness values, the choice fell on the heat treatments that last enough to be accurate, but not extremely time-consuming. The actual residual hardness values were checked on the grips of tensile samples, after the completion of the tensile tests. The results of hardness and tensile tests on the specimens belonging to the different hardness sets are reported in Table 2. To better appreciate the mechanical properties of AA2099 after overaging, Table 3 was added, reporting the numerical results of tensile tests on overaged AA2618 specimens, carried out by Ceschini et al. in [25]. Even if AA2618 is specifically designed to resist thermal exposure [25,29,30], the tensile properties of AA2099 after overaging were always slightly superior than that of AA2618 [25], even at the lower residual hardness conditions. Again, this is a promising indication for high temperature applications.

Target [HB]	**Overaging**	**Actual residual hardness [HB]**	**$R_{p0.2}$ [MPa] ±2σ**	**UTS [MPa] ±2σ**	**A_t[%] ±2σ**
164 (T83)	No overaging	165	619 (±7.2)	635 (± 4.7)	9.3 (±1.3)
147	6h @ 215°C	150	457 (±1.3)	531 (± 5.1)	8.1 (±1.7)
129	24h @ 215°C	135	379 (±2.1)	447 (±2.0)	11 (±2.4)
112	24h @ 245°C	115	263 (±8.2)	388 (±3.3)	16.6 (±1.5)
93	72h @ 245°C	93	194 (±4.2)	329 (±3.1)	18.9 (±3.3)
73	24h @ 305°C	75	120 (±3.7)	266 (±9.2)	20.7 (±1.7)

Table 2: Classes of hardness for AA2099 tensile specimens, overaging treatments performed to reach the targeted hardness, actual Brinell hardness measured after tensile tests and results of tensile tests on the overaged samples (average and standard deviation).

Target [HB]	**Overaging**	**Actual residual hardness [HB]**	**$R_{p0.2}$ [MPa]**	**UTS [MPa]**	**A_t[%]**
142 (T6)	No overaging	142	365	423	4.1
125	24 @ 200°C	126	317	384	5.8
115	10h @ 230°C	116	267	353	6.6
105	120h @ 230°C	104	218	321	6.6
90	3.5h @ 290°C	90	166	279	7.8
80	9h @ 305°C	79	121	245	10.2
70	30h @ 305°C	71	187	231	10.7

Table 3: Classes of hardness for AA2618 tensile specimens, overaging treatments performed to reach the targeted hardness, actual Brinell hardness measured after tensile tests and results of tensile tests on the overaged samples [25].

The relationships between tensile properties and residual hardness values of the alloy are reported in Fig.9a. As can be noted in Table 2, negligible differences between targeted and actual hardness

have been generally detected in the overaged samples. The actual residual Brinell hardness values were therefore taken into account in order to model the behaviour of the 2099 alloy with residual hardness. As expected, a well-defined relationship exists between tensile properties and residual hardness, as also reported by Jabra et al. [24]. In particular, as shown in Fig.9a, UTS and $Rp_{0.2}$ exhibit an exponential decrease in the overaged alloy, while A_t% shows a logarithmic increase with prolonged overaging. It is worth to underline the different behaviour of the AA2099 (Al-Cu-Li) alloy with respect to the AA2618 (Al-Cu-Mg-Ni-Fe) alloy [25], which display, respectively, an exponential and linear decrease of tensile properties with decreasing residual hardness.
Moreover, for each hardness class, the existing relationship of the average strength coefficient K and the average hardening coefficient n as a function of the residual material hardness is shown in Fig.9b. According to the experimental data, the strain hardening exponent is constantly growing for lower residual hardness, while the strengthening coefficient exhibits an opposite trend; both n and K follow a nearly linear function of residual hardness. The opposite trend of K and n as a function of residual hardness can be related to the microstructural modifications induced by the heat treatment conditions, as explained below.

- The very fine and coherent precipitates characterising the T83 condition (as clearly visible in Fig.7a) induce the maximum strengthening effect, which is directly translated into high values for K coefficient); however, these precipitates are not effective one step further the plastic field has been reached. Above the plastic threshold, the fine and coherent precipitates are cut according to the Ashby's model [31]. In case of the AA2099 alloy, given the almost total absence of secondary phases able to hinder the dislocations motion, deformation increases without appreciable strain hardening, and the strain hardening exponent is approximately null. This is confirmed by the almost horizontal trend of the stress-strain curves referring to T83 condition (reported as blue curves in Fig.10).

- On the contrary, the strengthening coefficient K progressively decreases for lower residual Brinell hardness, due to the coarsening of precipitates (whose evidences are reported in Fig.7b,c). At the same time, the strengthening exponent n is considerably increased due to the activation of the Orowan's mechanism [31]. In fact, the interaction between coarser, incoherent precipitates and dislocations is responsible for the growth of number of dislocations and their subsequent obstruction to slip.

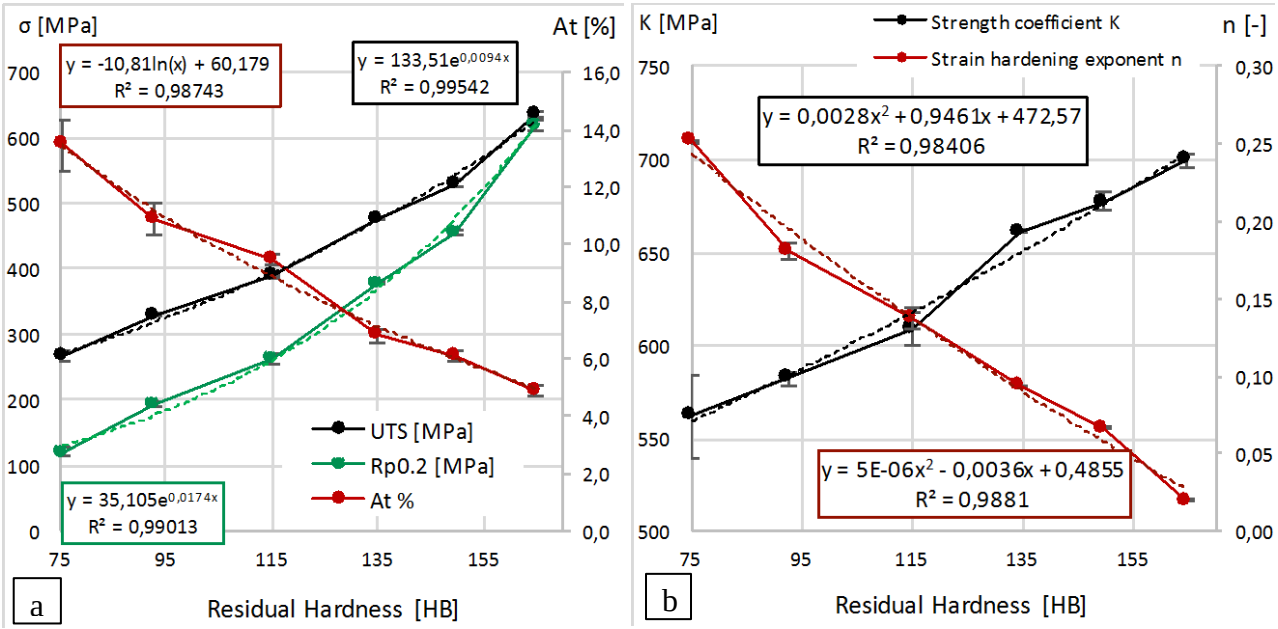

Figure 9: (a) Relationship between tensile properties (Proof Strength, Ultimate Tensile Strength, Elongation to failure) and residual hardness of AA2099; (b) relationship between strength coefficient K, strain hardening exponent n and residual hardness of the alloy. In both plots, each point is the average value of 3 tensile tests, while the error bars have been set as ±2σ.

Processing of the experimental data lead to the implementation of the following formula, which is able to predict the true stress of the alloy in the plastic field, as a function of the residual alloy hardness:

$$\sigma_{Hollomon} = (0.0028HB^2 + 0.9461HB + 472.57) \cdot \varepsilon_{plastic}^{(5\cdot10^{-6}HB^2 - 0.0036HB + 0.4855)}$$

Equation 3: Stress-strain model of 2099 alloy in the plastic field, as a function of the alloy residual hardness. The model is based on Hollomon's law, the strengthening coefficient K and the strain hardening exponent n being determined from elaboration of tensile tests data.

The validity of the model is confirmed by the fact that experimental results (dashed line in Fig.10) appropriately match the curves generated by the model (solid line in Fig.10). Absolute and relative errors were calculated for all hardness classes, as reported in Table 4. Due to the divergence of the modelled curves for high values of plastic deformation and in order to make an effective comparison between hardness classes, the experimental and modelled data were limited to $\varepsilon_{true} \leq 5\%$. It is possible to state that, with the exception of the peak aged condition, the maximum absolute error never reaches 30MPa. The relative error obviously tends to increase for the highly overaged conditions, due to the lower values of true stress. It is interesting to underline that the 93HB class exhibits a higher absolute error compared to 112 and 73HB classes and to compare the table to Fig.9b: the higher error value is mainly linked to the interpolation error in modelling the strain hardening exponent n. At the same time, it can be also pointed out that errors in K values modelling are not considerably affecting the modelling results (the low error for 112HB class is obtained through a nearly perfect interpolation of n value, but poor modelling of K value).

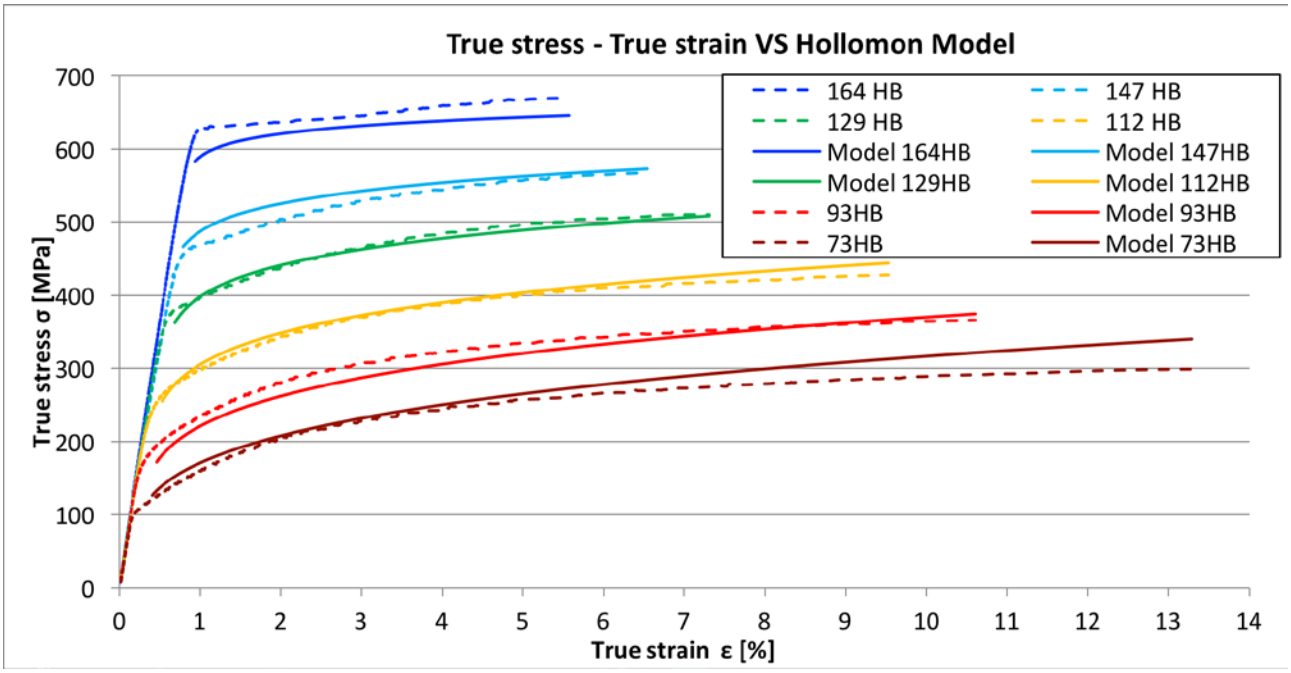

Figure 10: Actual true stress-true strain curves (dashed lines) compared to modelled curves (solid lines). The last ones have been calculated according to Hollomon's equation, therefore data are restricted to the plastic field. K and n parameters have been modelled as a function of residual hardness values, as reported in Fig.9b.

Error \ HB	164	147	129	112	93	73
Max absolute error [Mpa] $E_{abs} = \max(\lvert\sigma_{true\ i} - \sigma_{model\ i}\rvert)$	39	27	19	12	23	13
Corresponding relative error [%] $E_{rel} = \frac{\lvert\sigma_{true\ i} - \sigma_{model\ i}\rvert}{\sigma_{true\ i}}$	6,3%	5,7%	4,9%	4,5%	11,9%	9,0%

Table 4: Absolute and relative errors between true tensile data and the implemented Hollomon's model.

Finally, complementary SEM analyses of the fracture surfaces have been carried out on two tensile specimens, representative of the upper and lower residual hardness conditions: T83 and overaging for 24h at 305°C. The fracture surfaces of the tensile samples, reported in Fig.11, give evidence of microstructural changes affecting the alloy behaviour at different residual hardness values. Low magnification SEM micrograph of the T83 sample (Fig.11a) highlights the presence of shear lips, confirming the not negligible elongation to fracture (about 9%) reported in Table 2. High magnification SEM micrographs of the same T83 sample (Fig.11c) reveal a mixture of intergranular fracture and presence of fine dimples. The observations are in agreement with Lin et al. [20], whose TEM micrographs report the presence of continuous secondary phases and precipitate-free zone at grain boundaries, which act as stress concentration sites for crack initiation. The intergranular fracture mode in the peak-aged condition is also confirmed by others [3,27,32].

Overaging induces significant changes in the fracture mode. The fracture surface appear considerably deformed even at low magnification (Fig.11b).The high magnification micrograph (Fig.11d) gives evidence of very fine dimples, which cover the entire surface and which make grain boundaries no more perceivable. It seems that at peak hardness, the weak points are the grain boundaries, while in the overaged conditions, the material is weak both grain boundaries and the

interior of the grains because of the low density of precipitates. According to [20], also slight overaging (peak-aged condition with additional 48h at 152°C) results in coarsened, discontinuous, large-spaced grain boundary phases, which can therefore relieve stress concentration at grain boundaries, improving ductility. The observation is in agreement with our experimental data (Table 2), which highlight the nearly double elongation to fracture of the highly overaged condition, compared to the peak-aged condition.

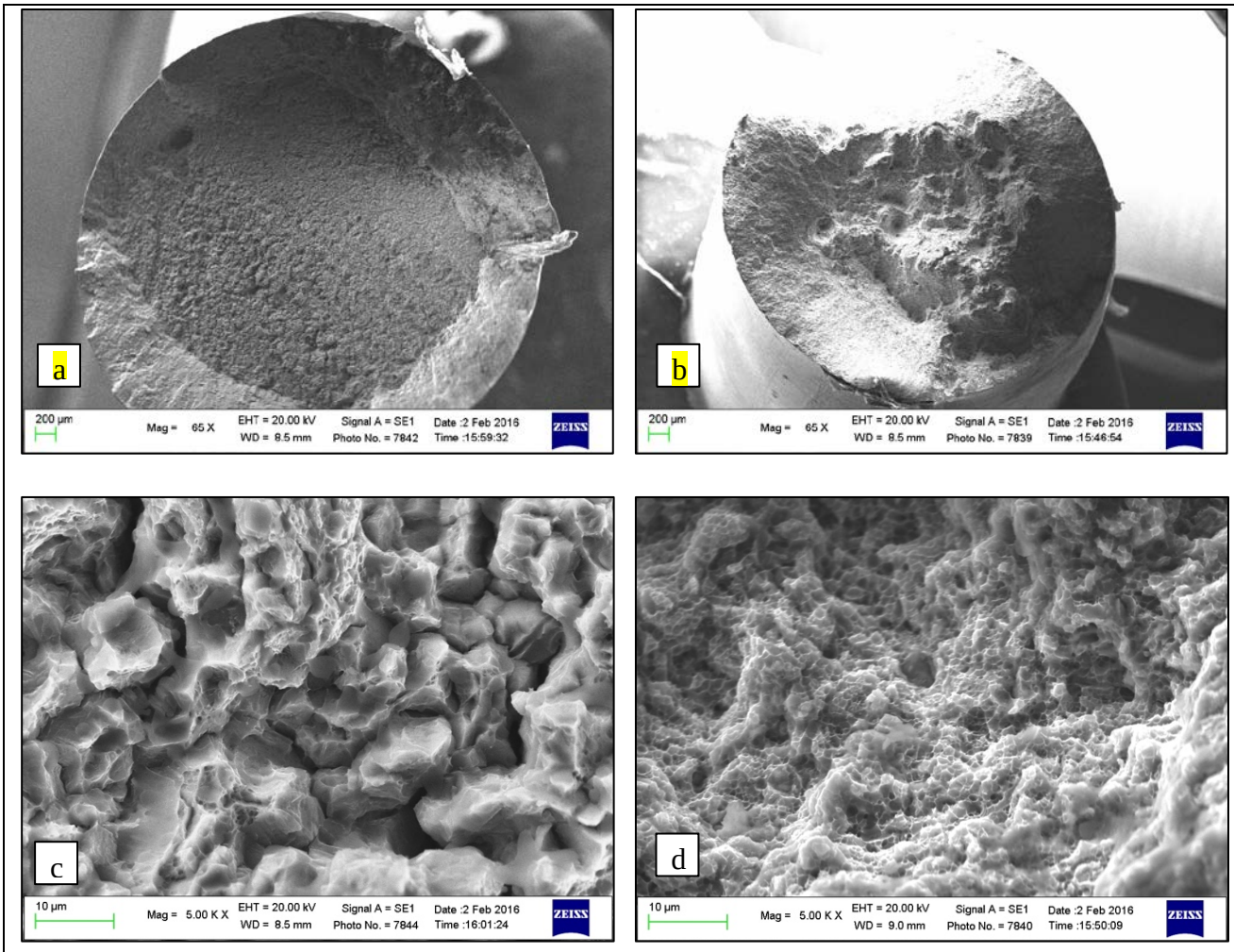

Figure 11: Low and high magnification micrographs of the fracture surfaces representative of (a), (c) the T83 condition, (b), (d) overaging to 75HB residual hardness; the significantly different fracture mechanisms is underlined.

4 Conclusions

With respect to other conventional Al alloys, AA2099 (Al-Cu-Li) exhibits a lower density and a higher elastic modulus, which provide an excellent specific stiffness at room temperature. The main strengthening mechanism of this alloy is precipitation hardening; however, similarly to other heat treatable Al alloys, also AA2099 undergoes coarsening of the strengthening precipitates during high temperature exposure, which can considerably reduce its performance. This study assessed the effect of overaging on the AA2099-T83, in the range 200-305°C, highlighting that:

- The lower the hardness, the lower the tensile strength of the alloy. To provide a useful instrument for the design process, the relation between residual hardness and tensile strength has been determined, according to Hollomon's equation in the plastic field.
- The lowest hardness and strength limit of AA2099 are reached after 24h at 305°C and it is maintained when the soaking time is further prolonged. This limit is comparable or even higher than that of Al alloys specifically designed for high temperature applications, which suggests that also 2099 might be suitable for high temperature applications.
- After thermal exposure, the main strengthening mechanism is provided by T_1 precipitates. T_1 phases tend to thicken at high temperatures but they do not dissolve, unlike ϑ', δ and S phases, while the formation of the coarse and not strengthening σ phase is activated. T_1 precipitation has therefore to be enhanced in order to promote the thermal stability of the 2099 Al alloy.

Overaging curves and room temperature tensile tests of overaged samples are the basic step to evaluate the suitability of the alloy for high temperature applications. Since Al-Cu-Li alloy AA2099 exhibited promising properties after overaging, even better than Al alloys specifically developed for high temperature applications, it is reasonable that also mechanical properties of AA2099 at high temperature would be encouraging.

Future work

Since the mechanical properties at high temperature are the key issue of automotive components operating at high temperature and the overaging results of AA2099 alloy are promising, the authors are currently involved in in testing the alloy at high temperature.

Acknowledgements

The authors gratefully acknowledge Ducati Spa for the support, Silvia Ming Zhu Sun for the substantial help in the experimental activities and Daniele Casari for his suggestions.

The JEOL JEM 2100F TEM are a part of the NORTEM infrastructure financed by the Research council of Norway, NTNU and SINTEF. The authors would like to thank the Research Council of Norway for funding through the FRINATEK project “Fundamental investigations of precipitation in the solid state with focus on Al-based alloys”

Bibliography

[1] C.J. Peel, B. Evans, C.A. Baker, D.A. Bennet, P.J. Gregson, H.M. Flower, The development of aluminium-lithium alloys, in: T.H. Sanders, E.A.J. Starke (Eds.), Alum. Alloy. II, Proc. 2nd Int. Alum. Conf. Monterey CA., 1984: pp. 363–392.

[2] R.J. Rioja, J. Liu, The evolution of Al-Li base products for aerospace and space applications, Metall. Mater. Trans. A Phys. Metall. Mater. Sci. 43 (2012) 3325–3337. doi:10.1007/s11661-012-1155-z.

[3] N.E. Prasad, A.A. Gokhale, P.R. Rao, Mechanical behaviour of aluminium – lithium alloys, Sadhana. 28 (2003) 209–246. doi:10.1007/BF02717134.

[4] Y. Ma, X. Zhou, G.E. Thompson, M. Curioni, P. Skeldon, X. Zhang, Z. Sun, C. Luo, Z. Tang, F. Lu, Anodic film growth on Al-Li-Cu alloy AA2099-T8, Electrochim. Acta. 80 (2012) 148–159. doi:10.1016/j.electacta.2012.06.126.

[5] E.A. Lindgren, L.P. Martin, M. Rosen, Characterization and Depth Profile of Lithium Depletion in Aluminum-Lithium Alloys by Ultrasound, in: D.O. Thompson, D.E. Chimenti (Eds.), Rev. Prog. Quant. Nondestruct. Eval., Plenum Press, New York, 1998: pp. 1435–1442.

[6] E.A. Starke, J.T. Staley, Application of modern aluminum alloys to aircraft, Prog. Aerosp. Sci. 32 (1996) 131–172. doi:10.1016/0376-0421(95)00004-6.

[7] W.X. Feng, E.S. Lin, E.A. Starke, The Effect of Minor Alloying Elements on the Mechanical Properties of Al-Cu-Li Alloys, Metall. Trans. A. 15 (1984) 1209–1220. doi:10.1007/BF02644715.

[8] C. Giumarra, B. Thomas, R.J. Rioja, New Aluminium Lithium Alloys for Aerospace Applications, in: Proc. Light Met. Technol. Conf. 2007, 2007.

[9] W.S. Miller, J. White, M.A. Reynolds, D.S. Mcdarmaid, G.M. Starr, Aluminium-Lithium-Copper-Magnesium-Zirconium Alloys with High Strength and High Toughness - Solving the Perceived Dichotomy, Le J. Phys. Colloq. 48 (1987) C3–151–C3–162. doi:10.1051/jphyscol:1987318.

[10] A. Smith, The Metallurgical Aspects of Aluminium-Lithium Alloys in Various Product Forms for Helicopter Structural Applications, J. Phys. Colloq. 48 (1987) 49–59.

[11] Y. Ma, X. Zhou, G.E. Thompson, T. Hashimoto, P. Thomson, M. Fowles, Distribution of intermetallics in an AA 2099-T8 aluminium alloy extrusion, Mater. Chem. Phys. 126 (2011) 46–53. doi:10.1016/j.matchemphys.2010.12.014.

[12] T. Warner, Recently-developed aluminium solutions for aerospace applictions, Mater. Sci. Forum. 519-521 (2006) 1271–1278.

[13] B. Decreus, A. Deschamps, F. De Geuser, P. Donnadieu, C. Sigli, M. Weyland, The influence of Cu/Li ratio on precipitation in Al-Cu-Li-x alloys, Acta Mater. 61 (2013) 2207–2218.

doi:10.1016/j.actamat.2012.12.041.

[14] J.F. Li, P.L. Liu, Y.L. Chen, X.H. Zhang, Z.Q. Zheng, Microstructure and mechanical properties of Mg, Ag and Zn multi-microalloyed Al-(3.2-3.8)Cu-(1.0-1.4)Li alloys, Trans. Nonferrous Met. Soc. China (English Ed. 25 (2015) 2103–2112. doi:10.1016/S1003-6326(15)63821-3.

[15] Z. Gao, J.-H. Chen, S.-Y. Duan, X.-B. Yang, C.-L. Wu, Complex Precipitation Sequences of Al-Cu-Li-(Mg) Alloys Characterized in Relation to Thermal Ageing Processes, Acta Metall. Sin. (English Lett. 29 (2016) 94–103. doi:10.1007/s40195-016-0366-5.

[16] C. Gao, Y. Luan, J.C. Yu, Y. Ma, Effect of thermo-mechanical treatment process on microstructure and mechanical properties of 2A97 Al-Li alloy, Trans. Nonferrous Met. Soc. China (English Ed. 24 (2014) 2196–2202. doi:10.1016/S1003-6326(14)63332-X.

[17] M.H. Tosten, J.M. Galbraith, P.R. Howell, Nucleation of δ’ (Al_3Li) on β' (Al_3Zr) in Al-Li-Zr and Al-Li-Cu-Zr alloys, J. Mater. Sci. Lett. 6 (1987) 51–53.

[18] D. Tsivoulas, P.B. Prangnell, The effect of Mn and Zr dispersoid-forming additions on recrystallization resistance in Al-Cu-Li AA2198 sheet, Acta Mater. 77 (2014) 1–16. doi:10.1016/j.actamat.2014.05.028.

[19] D. Tsivoulas, J.D. Robson, Heterogeneous Zr solute segregation and Al_3Zr dispersoid distributions in Al-Cu-Li alloys, Acta Mater. 93 (2015) 73–86. doi:10.1016/j.actamat.2015.03.057.

[20] Y. Lin, Z. Zheng, S. Li, X. Kong, Y. Han, Microstructures and properties of 2099 Al-Li alloy, Mater. Charact. 84 (2013) 88–99. doi:10.1016/j.matchar.2013.07.015.

[21] N. Brodusch, M. Trudeau, P. Michaud, L. Rodrigue, J. Boselli, R. Gauvin, Contribution of a New Generation Field-Emission Scanning Electron Microscope in the Understanding of a 2099 Al-Li Alloy, Microsc. Microanal. Off. J. Microsc. Soc. Am. Microbeam Anal. Soc.

Microsc. Soc. Canada. (2012) 1. doi:10.1017/S143192761200150X.

[22] D. Ortiz, J. Brown, M. Abdelshehid, P. DeLeon, R. Dalton, L. Mendez, J. Soltero, M. Pereira, M. Hahn, E. Lee, J. Ogren, R. Clark, J. Foyos, O.S. Es-Said, The effects of prolonged thermal exposure on the mechanical properties and fracture toughness of C458 aluminum-lithium alloy, Eng. Fail. Anal. 13 (2006) 170–180. doi:10.1016/j.engfailanal.2004.10.008.

[23] M. Romios, R. Tiraschi, C. Parrish, H.W. Babel, J.R. Ogren, O.S. Es-Said, Design of Multistep Aging Treatments of 2099 (C458) Al-Li Alloy, J. Mater. Eng. Perform. 14 (2005) 641–646. doi:10.1361/105994905X64594.

[24] J. Jabra, M. Romios, J. Lai, E. Lee, M. Setiawan, E.W. Lee, J. Witters, N. Abourialy, J.R. Ogren, R. Clark, T. Oppenheim, W.E. Frazier, O.S. Es-Said, The Effect of Thermal Exposure on the Mechanical Properties of 2099-T6 Die Forgings, 2099-T83 Extrusions, 7075-T7651 Plate, 7085-T7452 Die Forgings, 7085-T7651 Plate, and 2397-T87 Plate Aluminum Alloys, J. Mater. Eng. Perform. 15 (2006) 601–607. doi:10.1361/105994906X136142.

[25] L. Ceschini, Al. Morri, An. Morri, M. Di Sabatino, Effect of thermal exposure on the residual hardness and tensile properties of the EN AW-2618A piston alloy, Mater. Sci. Eng. A. 639 (2015) 288–297. doi:10.1016/j.msea.2015.04.080.

[26] J.H. Hollomon, Trans. AIME. 162 (1945) 268–290.

[27] R. Doglione, Le leghe Alluminio-Litio, Metall. Ital. 97 (2005) 39–50.

[28] J. Chen, Ductile tearing of AA2198 aluminium-lithium sheets for aeronautic application, Ecole Nationale Superieure des Mines de Paris, 2012.

[29] E. Balducci, L. Ceschini, A. Morri, A. Morri, M. Di, L. Arnberg, Y. Li, High temperature behavior of the EN AW-2618A piston alloy containing 0.12wt % Zr : influence of heat treatment, Mater. Today Proc. doi:10.1016/j.matpr.2015.10.094.

[30] F. Nový, M. Janeček, R. Král, Microstructure changes in a 2618 aluminium alloy during

ageing and creep, J. Alloys Compd. 487 (2009) 146–151. doi:10.1016/j.jallcom.2009.08.014.

[31] G.E. Dieter, Mechanical Metallurgy, McGraw-Hil, 1986.

[32] W. Miller, J. White, D. Lloyd, The Physical Metallurgy of Aluminium-Lithium-Copper-Magnesium-Zirconium Alloys-8090 and 8091, J. Phys. Colloq. 48 (1987) 139–149.

[33] S.C. Wang, M.J. Starink, Precipitates and intermetallic phases in precipitation hardening Al–Cu–Mg–(Li) based alloys, Int. Mater. Rev. 50 (2005) 193–215. doi:10.1179/174328005X14357.

[34] H. Li, Y. Tang, Z. Zeng, Z. Zheng, F. Zheng, Effect of ageing time on strength and microstructures of an Al-Cu-Li-Zn-Mg-Mn-Zr alloy, Mater. Sci. Eng. A. 498 (2008) 314–320. doi:10.1016/j.msea.2008.08.001.